ACS APPLIED MATERIALS & INTERFACES

Research Article

www.acsami.org

Starfish-shaped $Co_3O_4/ZnFe_2O_4$ Hollow Nanocomposite: Synthesis, Supercapacity, and Magnetic Properties

Xiao-Wei Hu, Sheng Liu, Bo-Tao Qu, and Xiao-Zeng You*

State Key Laboratory of Coordination Chemistry, School of Chemistry and Chemical Engineering, Collaborative Innovation Center of Advanced Microstructures, Nanjing University, Nanjing 210093, P. R. China

Supporting Information

ABSTRACT: A novel starfish-shaped porous $Co_3O_4/ZnFe_2O_4$ hollow nanocomposite was fabricated for the first time by a facile and stepwise hydrothermal approach, utilizing metal−organic frameworks as precursors and sacrificial templates. The morphology evolution in the synthetic process upon reaction time and amount of raw materials were investigated in detail. The as-synthesized starfish-shaped porous $Co_3O_4/ZnFe_2O_4$ composites were studied as an electrode material for supercapacitors showing good capacitive performances. Their specific capacitance can reach as high as 326 F g^{-1} at 1 A g^{-1}. The rational combination of components with different potential windows in a composite material enables a wide overall potential range resulting in the highest energy density of 82.5 Wh kg^{-1}, significantly larger than that of the single components. Magnetic measurements show that the system presents a large coercivity and high squareness (at 1.8 K, H_c = 884 Oe and M_r/M_s = 0.52) with respect to the individual components, which may be attributed to the unique morphology of $Co_3O_4/ZnFe_2O_4$, as well as surface and interface exchange coupling effects. Materials with this novel design and fabrication may show promise for potential applications in electrochemical energy storage and magnetic devices.

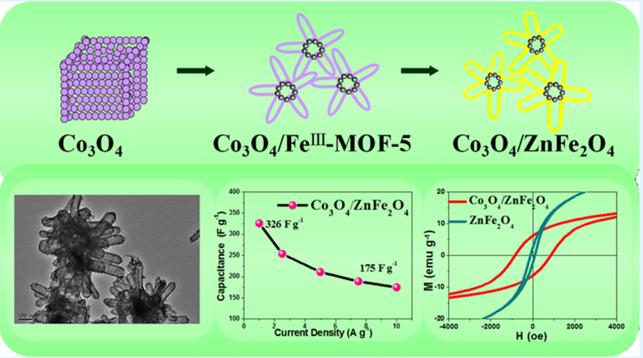

KEYWORDS: *starfish-shaped $Co_3O_4/ZnFe_2O_4$ nanocomposites, hollow, porous, supercapacitor, bimagnetic system, magnetic*

INTRODUCTION

In recent years, the increasing demand for sustainable and clean energy has attracted considerable attention toward developing efficient energy storage systems. Much research effort has been aimed at supercapacitors which can provide energy densities orders of magnitude higher than dielectric capacitors, as well as greater power densities and longer cycle lives than that of batteries.[1−5] Among the electrode materials studied for supercapacitors, transitional metal oxides (RuO_2,[6] MnO_2,[7] Co_3O_4,[8] NiO,[9] etc.) have been widely investigated because of their high pseudocapacitances from the reversible redox reactions. These metal oxides normally have their own limited potential windows in certain electrolytes.[10] The charge storage efficiency drops dramatically when the potential window expands. On the basis of the energy density equation below:

$$E = \frac{1}{2}CV^2$$

where E is the energy density, C is the specific capacitance, and V is the potential window, in order to achieve a large energy density, not only a high specific capacitance is needed, but also a wide potential window. Therefore, combining different metal oxides with complementary potential windows in the same electrolyte seems to be a reasonable approach to obtain great energy density. Previous studies have focused a lot on asymmetric supercapacitors, which integrate anodes and cathodes of different potential windows generating a large overall operating voltage.[11,12] However, research on a single electrode material of mixing metal oxides fulfilling the same purpose have not been well explored.

In the past decade, metal−organic frameworks (MOFs) have received intensive attention because of their large specific area, ultrahigh porosity, and various applications, including gas storage/separation, in catalysis, as chemical sensors, and so on.[13−18] Inspired by their diverse configurations, scientists have utilized MOF materials as precursors or templates to explore a novel path preparing porous nanomaterials for energy storage systems.[19−23] For example, Guo et al. prepared porous Co_3O_4 material by a simple solid-state thermolysis of the Co-based MOF, which displayed a specific capacitance of 150 F g^{-1} at 1 A g^{-1} in 2 M KOH electrolyte.[24] Moreover, porous ZnO/$ZnFe_2O_4$/C octahedra can be fabricated using MOF as both the precursor and the self-sacrificing template showed greatly enhanced performance of Li^+ storage when tested as anode materials for lithium-ion batteries.[25]

Received: March 16, 2015
Accepted: April 16, 2015
Published: April 16, 2015

DOI: 10.1021/acsami.5b02317
ACS Appl. Mater. Interfaces 2015, 7, 9972−9981

Scheme 1. Synthesis Procedure of the Starfish-Shaped Porous $Co_3O_4/ZnFe_2O_4$ Hollow Nanocomposite

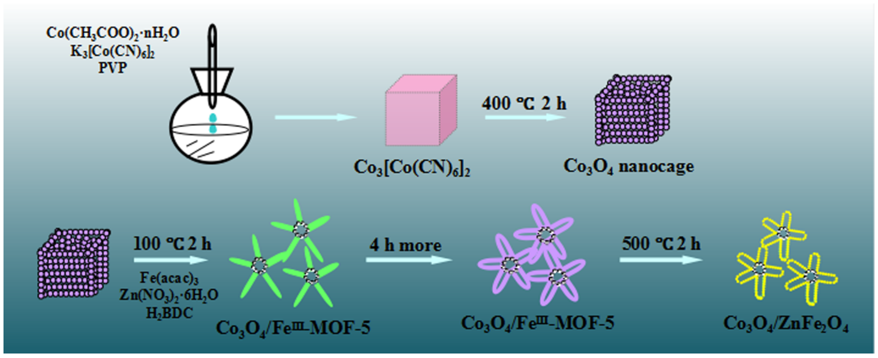

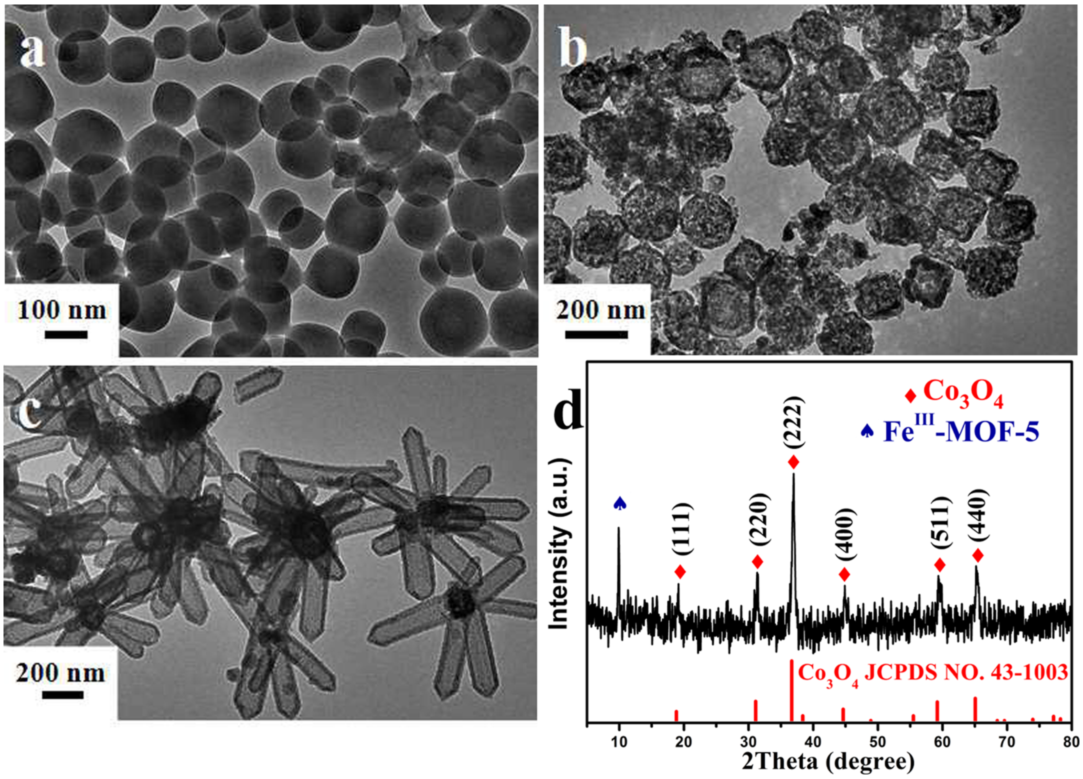

Figure 1. TEM image of (a) $Co_3[Co(CN)_6]_2 \cdot nH_2O$ nanoparticles; (b) Co_3O_4 nanocages; (c) Co_3O_4/ Fe^{III}-MOF-5; and (d) XRD pattern of Co_3O_4/Fe^{III}-MOF-5.

Herein we report a stepwise strategy to design and fabricate novel starfish-shaped porous $Co_3O_4/ZnFe_2O_4$ hollow nanocomposites from MOF precursors as supercapacitor electrode material forming a wide potential window from −0.85 to 0.50 V (vs Hg/HgO in 6 M KOH). In the starfish-shaped structure, the Co_3O_4 nanocages act as the "starfish head" and porous nanotubes composed of $ZnFe_2O_4$ nanoparticles from the partial Fe(III) substituted MOF-5 (Fe^{III}-MOF-5) act as the "starfish arms". The nanocomposite showed the specific capacitance as high as 326.7 F g^{-1}, while its energy density reached 82.5 Wh K g^{-1} at the power density of 675 W kg^{-1} due to the enlarged potential window. All these results are significantly promoted from those of the individual components. Meanwhile, we ran the magnetic measurements for the as-synthesized $Co_3O_4/ZnFe_2O_4$ composites revealing it to be with much larger magnetic hysteresis loops at 1.8 K compared with $ZnFe_2O_4$. On account of these discoveries, our starfish-shaped porous $Co_3O_4/ZnFe_2O_4$ hollow nanocomposites are believed to have potential applications in electrochemical energy storage and magnetic devices.

EXPERIMENTAL SECTION

Preparation of the Starfish-Shaped Co_3O_4/Fe^{III}-MOF-5 Hollow Nanocomposites. All the solvents and chemicals were of analytical purity and used without further purification. The porous Co_3O_4 nanocages were prepared according to a previous work.[26] To obtain the starfish-shaped Co_3O_4/Fe^{III}-MOF-5, Co_3O_4 nanocages (25 mg) were dissolved in 2 mL DMF-ethanol mixture solution (v/v = 5/3) and sonicated for 30 min at room temperature. Then, 75 mg $Fe(acac)_3$, 58 mg $Zn(NO_3)_2 \cdot 6H_2O$ and 12 mg H_2BDC were added to the above solution under sonication. The mixed solution was transferred to a 50 mL Teflon autoclave afterward. The sealed vessel was heated at 100 °C for 6 h before cooling down to room temperature.[27] The starfish-shaped Co_3O_4/Fe^{III}-MOF-5 hollow nanocomposites were obtained after centrifugation and washing of several times.

Preparation of the Starfish-Shaped $Co_3O_4/ZnFe_2O_4$ Hollow Nanocomposites. The starfish-shaped $Co_3O_4/ZnFe_2O_4$ hollow

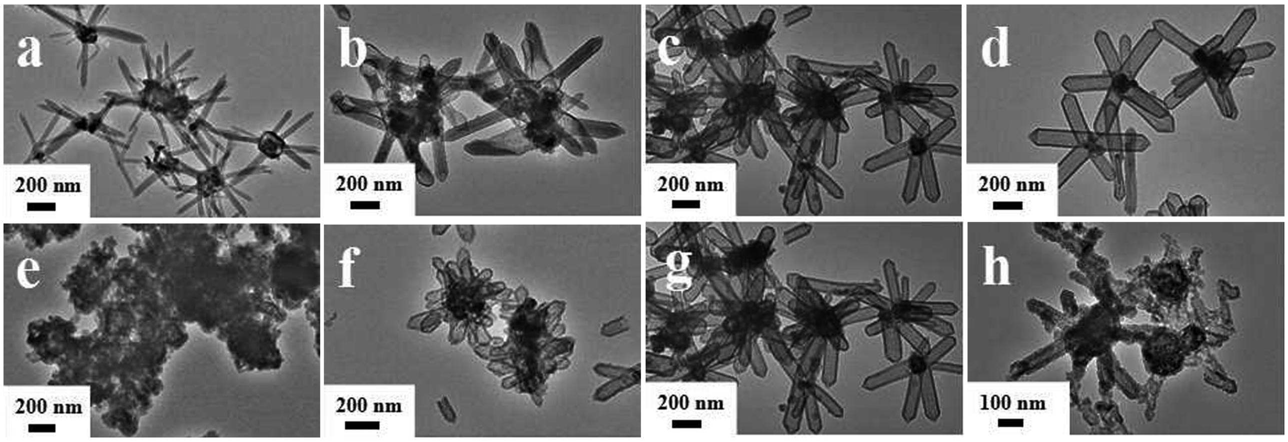

Figure 2. TEM image of Co_3O_4/Fe^{III}-MOF-5 prepared with different grown condition (a) 2 h; (b) 3 h; (c) 6 h; (d) 8 h; (e) 5 mg; (f) 15 mg; (g) 25 mg; and (h) 35 mg.

nanocomposites were obtained by a simple heating process of the as-synthesized Co_3O_4/Fe^{III}-MOF-5 in the tube furnace in air at 500 °C for 2 h with a heating rate of 1 °C min^{-1}.

Materials Characterization. Powder X-ray diffraction patterns (XRD) were obtained with a Bruker D8 Advance X-ray powder diffractometer with Cu K_α radiation (λ = 1.5406 Å) between 5° and 80° at scanning rate of 2° min^{-1}. The morphology of the synthesized products was analyzed using the transmission electron microscopy (TEM, JEM-2100, JEOL) with an accelerating voltage of 200 kV. The specific porous structural features of the as-prepared Co_3O_4/$ZnFe_2O_4$ were determined using a Brunauer−Emmett−Teller (BET) surface analyzer (Micromeritics ASAP 2020 M+C volumetric adsorption Equipment). X-ray photoelectron spectroscopy (XPS) were investigated by a PHI 5000 Versaprobe X-ray photoelectron spectrometer.

Electrochemical and Magnetic Measurements. The working electrode was fabricated by mixing 80 wt % active materials, 15 wt % acetylene black, and 5 wt % poly(vinylidene fluoride) (PVDF) binder. The resulting mixture paste was painted on the stainless steel mesh and dried at 120 °C for 12 h in vacuum oven. All electrochemical measurements were carried out on CHI 660D electrochemical workstation (CH Instruments) using a three-electrode system at room temperature using 6 M KOH as electrolyte. The counter electrode and reference electrode were platinum foil (1 cm^2) and Hg/HgO electrode, respectively. The electrochemical impedance spectroscopy (EIS) was conducted in the frequency range between 100 kHz and 0.01 Hz with a perturbation amplitude of 5 mV vs open-circuit potential. Magnetic measurements were conducted using a Quantum Design MPMS XP-5 superconducting quantum interference device (SQUID).

■ RESULTS AND DISCUSSION

As illustrated in Scheme 1, the starfish-shaped Co_3O_4/Fe^{III}-MOF-5 composites were synthesized from the Fe^{III}-MOF-5 formation on Co_3O_4 nanocages by the addition of Fe, Zn precursors and H_2BDC. With reaction time increasing, Fe^{III}-MOF-5 turned into a nanotube structure. After a simple calcination process, Co_3O_4/$ZnFe_2O_4$ hollow nanocomposites were obtained by a self-sacrificial templating approach (details in the Experimental Section).

Morphology and Structure of the Starfish-Shaped Co_3O_4/Fe^{III}-MOF-5 Hollow Nanocomposites. The morphology of the as-prepared products was observed using TEM. Figure 1a shows that the $Co_3[Co(CN)_6]_2 \cdot nH_2O$ nanoparticles are uniform in both size and shape with a diameter around 200 nm. From the image of the Co_3O_4 nanocages in Figure 1b, we can see after the calcination at 400 °C for 2 h, hollow structures of the similar shape were obtained. The structure of the starfish-shaped Co_3O_4/Fe^{III}-MOF-5 is shown in Figure 1c. It can be noticed that several Fe^{III}-MOF-5 nanotubes grow out from one Co_3O_4 hollow nanocage to form a “starfish” shape. All the nanotubes have a well distributed morphology with diameter of 100 nm, length around 400 nm and shell thickness of 10 nm. The powder X-ray diffraction (PXRD) pattern of the starfish-shaped Co_3O_4/Fe^{III}-MOF-5 (Figure 1d) matches well with that of Co_3O_4 (JCPDS:43-1003) and Fe^{III}-MOF-5 (blue spade) from previous literature,[27] indicating the successful synthesis of Co_3O_4/Fe^{III}-MOF-5.

Growth Process of Co_3O_4/Fe^{III}-MOF-5 Hollow Nanocomposites. Furthermore, to meticulously investigate the morphology evolution process of the starfish-shaped Co_3O_4/Fe^{III}-MOF-5 hollow nanocomposite, we conduct a series of controlled experiments upon reaction time and the added Co_3O_4 nanocages amount.

Figure 2a−d presents the typical morphology of the products for various reaction times. It gave us a brief impact on how the nanocomposite gradually evolved. With a short 2 h time of reaction, the morphology of the as-obtained Fe^{III}-MOF-5 are sword-shaped nanobelts, shown in Figure 2a. When the reaction time further increased to 3 h, the nanobelt structures were converted to hollow structures from outside (sword point) (Figure 2b). A complete formation of Fe^{III}-MOF-5 hollow nanocomposites occurred after 6 h reaction (Figure 2c). The Co_3O_4 nanocages were uniformly covered by the Fe^{III}-MOF-5 nanotubes with diameters of 100 nm, lengths up to 400 nm and shell thickness of 10 nm. When the synthesis process was carried out even longer (8 h), the morphology of Co_3O_4/Fe^{III}- MOF-5 remained the same (Figure 2d).

On the basis of the above study, we suggest a structure formation process as follows: Co_3O_4 nanocages were acting as seeds on which the Fe^{III}-MOF-5 could grow. Because of the presence of Co_3O_4 nanocages, the Fe^{III}-MOF-5 nucleated from the surface of the Co_3O_4 nanocages to one certain direction outward. Noticing that the Fe^{III}-MOF-5 possessed a sword shape with a relatively dark inside (Figure 2a), we know that high surface-energy faces were formed as mentioned in the previous literature.[27] With the increasing reaction time, the formation of nanotubes took place in order to reduce the surface energy starting from the “sword points” (Figure 2b,c). When the reaction time continued to increase, the nanocomposite morphology remained the same, indicating a complete conversion.

Amount of Co_3O_4 added is another key factor in the synthesis of Co_3O_4/Fe^{III}-MOF-5. Figure 2(e−h) showed the TEM images of Co_3O_4/Fe^{III}-MOF-5 prepared in different Co_3O_4 additions. When only 5 mg Co_3O_4 was added, there was not enough space on the Co_3O_4 nanocages for all Fe^{III}-MOF-5 precursors to grow into nanotubes, hence the starfish-shaped morphology did not appear (Figure 2e). However, the fact that Fe^{III}-MOF-5 mostly distributed around the Co_3O_4 nanocages was clear evidence to support our proposed growth mechanism that Fe^{III}-MOF-5 tended to nucleate from the Co_3O_4 nanocages. With the Co_3O_4 amount increased to 15 mg, nanotube structures began to appear, as shown in Figure 2f. Compared to the fully grown nanotubes in Figure 2g (the same as those in Figure 2c), it is obvious that more Fe^{III}-MOF-5 nanotubes grew from one Co_3O_4 nanocage because of the higher (Zn + Fe)/Co ratio. If more Co_3O_4 (35 mg) were involved, then the nanotube structure became vague, as shown in Figure 3h, which should arise from the incomplete growth of Fe^{III}-MOF-5 nanotubes in a small (Zn + Fe)/Co ratio. The above discussion illustrates how the reaction time and Co_3O_4 amount can affect the structure formation. With the varying conditions, the starfish-shaped morphology only takes place in a suitable reaction time and (Zn + Fe)/Co ratio.

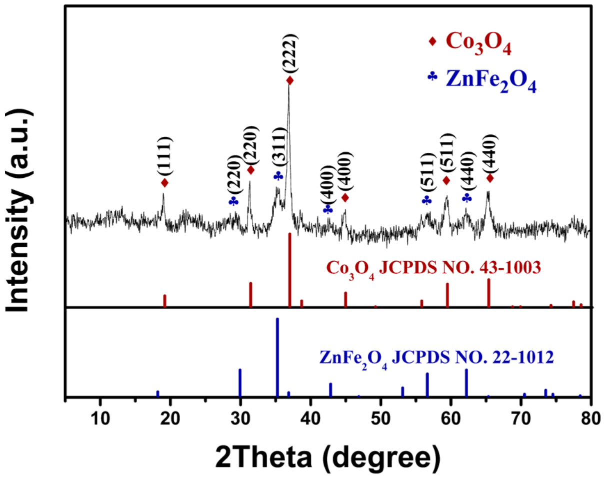

Figure 3. XRD pattern of Co_3O_4/$ZnFe_2O_4$.

Morphology and Structure of the Starfish-Shaped Porous Co_3O_4/$ZnFe_2O_4$ Hollow Nanocomposites. The Co_3O_4/$ZnFe_2O_4$ hollow nanocomposites were obtained after a calcination process of the starfish-shaped Co_3O_4/Fe^{III}-MOF-5. The crystallite phase purity of as-made product was further analyzed by XRD. The Co_3O_4/$ZnFe_2O_4$ shows a mixed XRD pattern of $ZnFe_2O_4$ (JCPDF #22-1012)[28] and Co_3O_4 (JCPDF #43-1003)[29] in Figure 3, in agreement with the preparation process. Compared with Figure 1d, the characteristic peaks of cubic crystalline MOF-5 at 9.7° disappeared in Figure 3. This indicates that Co_3O_4/Fe^{III}-MOF-5 was completely transformed to Co_3O_4/$ZnFe_2O_4$ after the annealing process.

Figure 4a shows the TEM image of the Co_3O_4/$ZnFe_2O_4$ nanocomposite, and we can see that the starfish-shaped hollow structure is well maintained after calcination, while the nanotubes become highly porous, consisting of numerous $ZnFe_2O_4$ nanocrystals of 10 nm (Figure 4b). It is not hard to realize that in the conversion from Co_3O_4/Fe^{III}-MOF-5 to Co_3O_4/$ZnFe_2O_4$, most of the carbon in Fe^{III}-MOF-5 was oxidized into gases, leading to the porous structure formation.

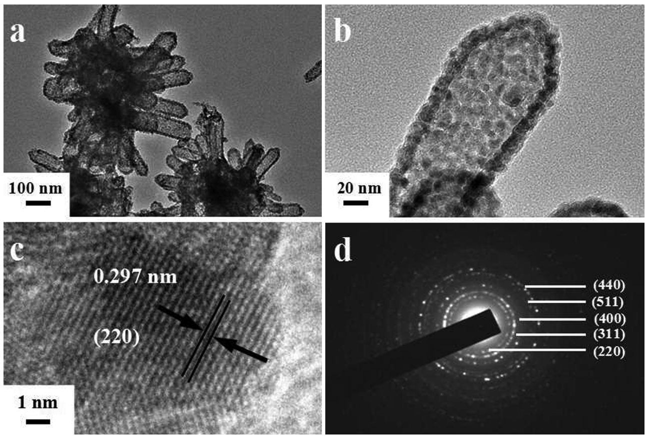

Figure 4. TEM image of (a) Co_3O_4/$ZnFe_2O_4$ hollow nanocomposites, (b) a single $ZnFe_2O_4$ nanotube, (c) High resolution TEM lattice image of a $ZnFe_2O_4$ nanoparticle, and (d) SAED patterns of the $ZnFe_2O_4$ nanotube.

Interestingly, even after a long sonication time for the samples, the $ZnFe_2O_4$ porous nanotubes can still remain closely attached to the Co_3O_4 nanocages, suggesting strong interactions between them. The marked *d*-spacing of 0.297 nm in a high-resolution TEM lattice image of an individual $ZnFe_2O_4$ nanoparticle (Figure 4c) matches well to the *d*-spacing of (220) plane of $ZnFe_2O_4$ (JCPDF #22-1012), consistent with the peak observed in the XRD characterization. Additionally, the corresponding selected area electron diffraction (SAED) pattern reveals the polycrystalline nature of the $ZnFe_2O_4$ nanotubes with the diffraction rings matched well with the (220), (311), (400), (511), and (440) planes of the $ZnFe_2O_4$ (JCPDF # 22-1012).

The elements' chemical states are further verified by X-ray photoelectron spectroscopy (XPS). As shown in Figure 5a, there are two main peaks with binding energies at 779.1 eV (Co $2p_{3/2}$) and 794.0 eV (Co $2p_{1/2}$) in the Co 2p XPS spectra. These results demonstrate that cobalt exists in the form of Co_3O_4.[30] The Fe 2p XPS pattern (Figure 5b) shows two peaks (724.7 and 710.5 eV) matching the binding energy of Fe $2p_{1/2}$ and Fe $2p_{3/2}$ and a small satellite peak in between, which evidenced the presence of Fe(III) species.[31]

The XPS spectrum of Zn 2p is displayed in Figure 5c. Its XPS peaks are centered at about 1021 and 1044 eV, respectively, corresponding to Zn(II) species.[32] The existence of trace amounts of carbon (0.28% weight percentage in elemental analysis) was also found in Figure 6d from the calcination residual of the organic frameworks.[33]

The nitrogen adsorption and desorption measurements were performed to estimate the Brunauer−Emmett−Teller (BET) surface area and pore size distribution of the porous Co_3O_4/$ZnFe_2O_4$ hollow nanostructures. As shown in Figure 6, the isotherm of the porous Co_3O_4/$ZnFe_2O_4$ nanocomposites exhibits a hysteresis loop at p/p_0 of 0.6, indicating the presence of mesopores.[34,35] The BET specific surface area of the starfish-shaped porous Co_3O_4/$ZnFe_2O_4$ nanostructure was calculated to be 46.2 $m^2\ g^{-1}$. The pore-size distribution (Figure 6, inset) reveals a narrow unimodal distribution centered at 10 nm, which can be attributed to the porous shell. The results are in good agreement with the value determined from the high-magnification TEM images, as discussed above.

Electrochemical Performances of Starfish-Shaped Porous Co_3O_4/$ZnFe_2O_4$ Nanocomposites. To evaluate

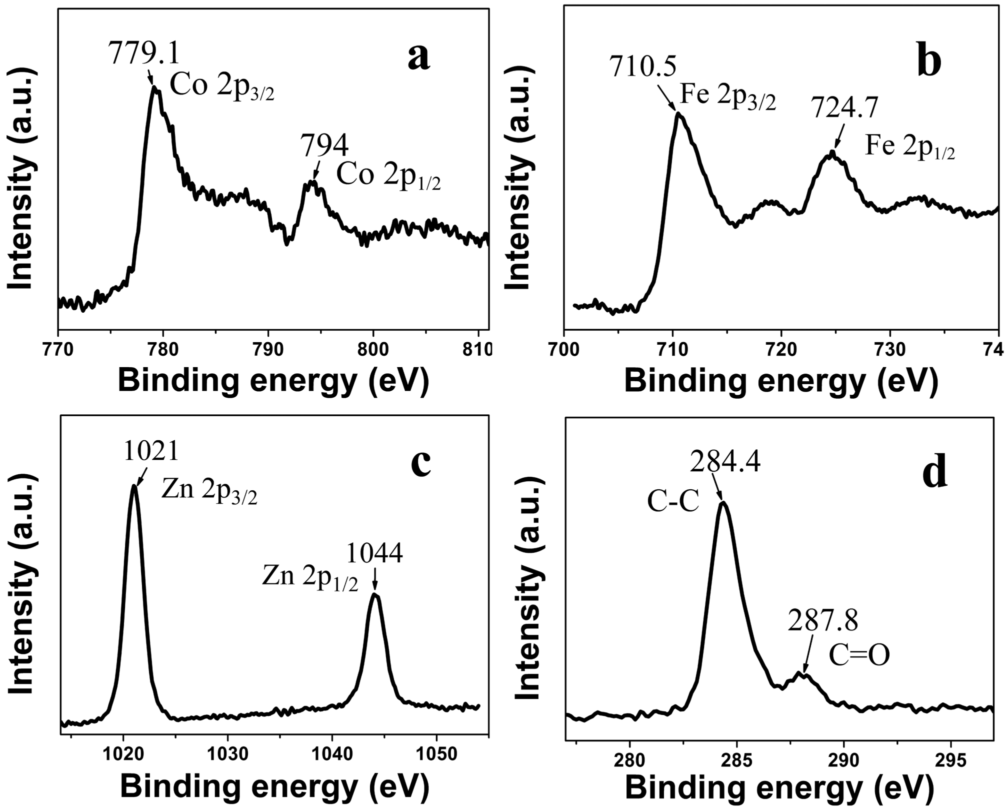

Figure 5. XPS of Co 2p (a), Fe 2p (b), Zn 2p (c), and C 1s (d) in $Co_3O_4/ZnFe_2O_4$ nanocomposites.

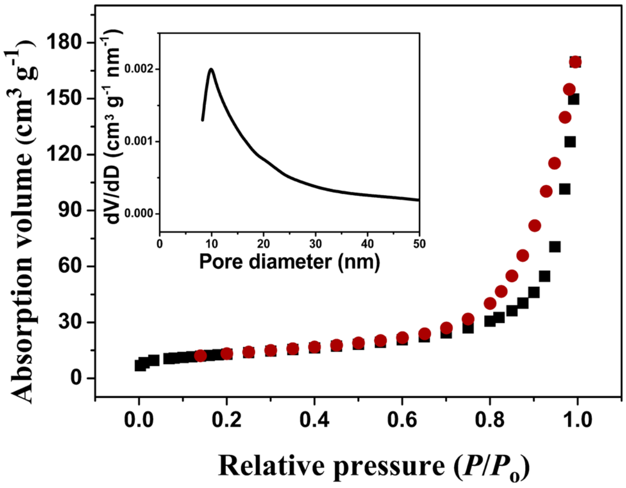

Figure 6. N_2 adsorption/desorption isotherm curve for the starfish-shaped porous $Co_3O_4/ZnFe_2O_4$ hollow nanocomposites. Inset: The pore size distribution of $Co_3O_4/ZnFe_2O_4$ nanocomposites.

their capacitive performances, the control Co_3O_4 nanocages, $ZnFe_2O_4$ hollow spheres (see Supporting Information, SI) and starfish-shaped porous $Co_3O_4/ZnFe_2O_4$ hollow nanocomposites were fabricated into supercapacitor electrodes for electrochemistry studies.

Figure 7 depicts typical cyclic voltammograms (CV) curves of the three electrodes at sweeping rate of 5 mV s^{-1}. The CV curves of Co_3O_4 nanocages in Figure 7 are nearly symmetrical with redox peaks belonging to the reversible reactions between different Co valence states. However, $ZnFe_2O_4$ shows its good charge storage properties mainly in the negative potential range due to the redox reactions of Fe(III) to Fe(II). The CV curve of starfish-shaped porous $Co_3O_4/ZnFe_2O_4$ nanocomposites combines that of Co_3O_4 and $ZnFe_2O_4$ with some peak shifts observed. This phenomenon is not rare in asymmetric supercapacitor studies. When mixing metal oxides with their own redox reactions together into one device, the situation of peak shift and peak disappearance occasionally happened.[36,37] Similar results have also been found in previous single electrode supercapacitor reports studying bimetallic oxides when varying the metal/metal ratio.[38] However, the underlying electrochemistry mechanism here still needs more detailed research to reveal.

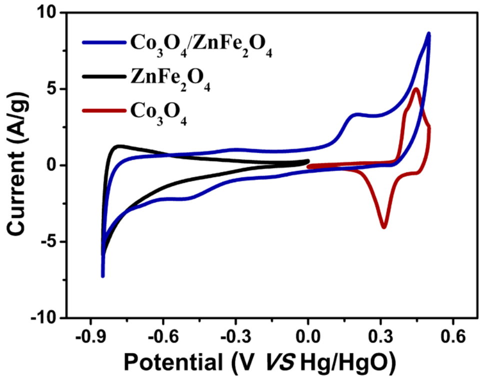

Figure 7. CV curves of different electrodes in 6 M KOH electrolyte at 5 mV s^{-1}.

To learn about the charge storage capacity of the electrodes, galvanostatic charge/discharge measurements were carried out at current densities from 1 to 10 A g^{-1}, as shown in Figure 8. Both Co_3O_4 and $ZnFe_2O_4$ curves are quite symmetric during charge and discharge process, indicating reversible redox

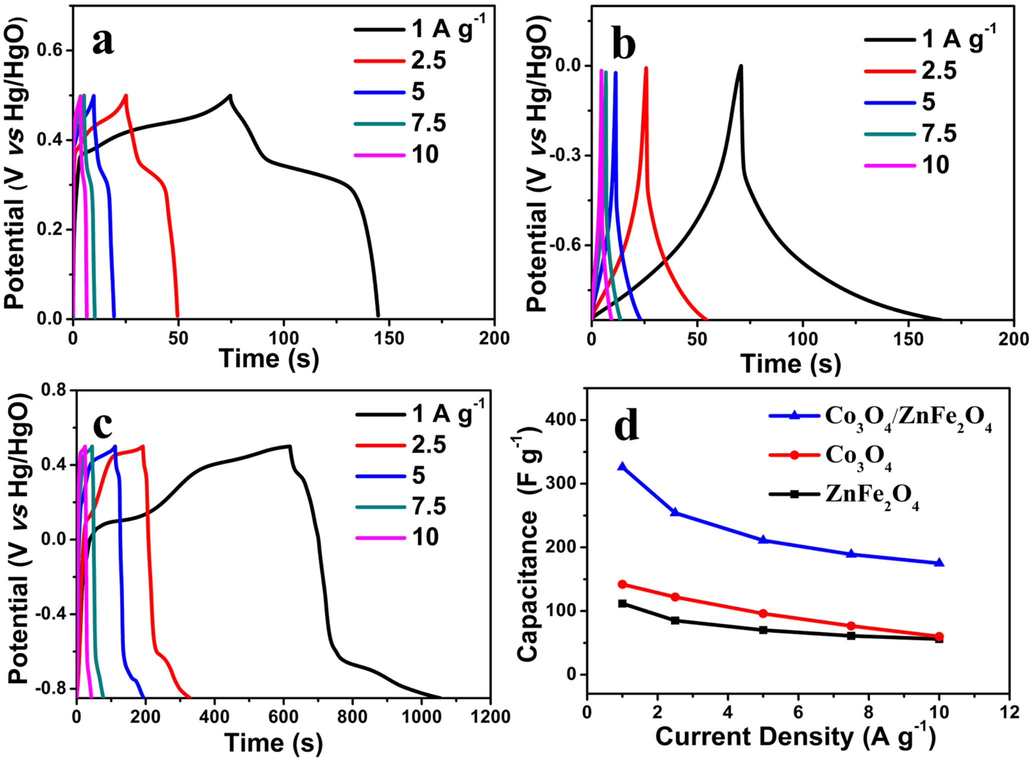

Figure 8. Gravimetric capacitance of (a) Co_3O_4, (b) $ZnFe_2O_4$, (c) $Co_3O_4/ZnFe_2O_4$, and (d) their rate performances at different current densities.

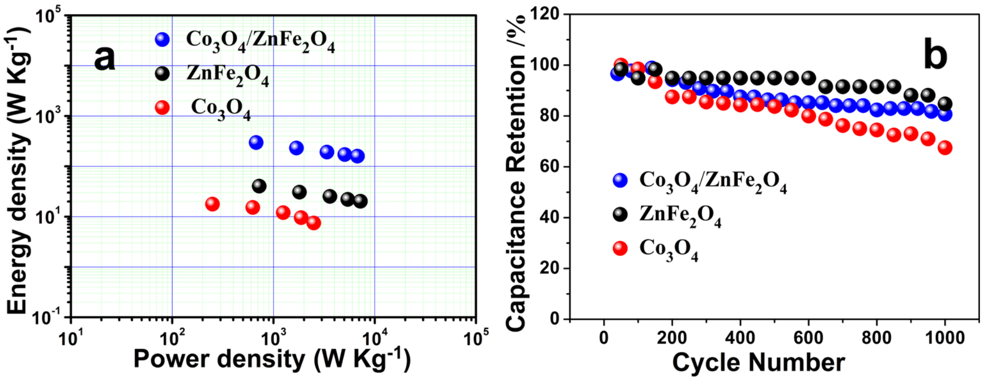

Figure 9. Ragone plots (a) and cycling performance (b) of Co_3O_4, $ZnFe_2O_4$ and $Co_3O_4/ZnFe_2O_4$ electrodes.

reactions and good pseudocapacitive feature. In Figure 8c, the discharge curve of $Co_3O_4/ZnFe_2O_4$ electrode is significantly longer than the previous two electrodes, representing a higher specific capacitance. All the platforms in the charge and discharge curves match well with the peaks shown in the CV (Figure 7).

The highest specific capacitance obtained for $Co_3O_4/ZnFe_2O_4$ is 326.7 F g^{-1} at 1 A g^{-1}, which is much higher than that of the Co_3O_4 (142 F g^{-1}) and $ZnFe_2O_4$ (112 F g^{-1}). The rate performances for electrodes at various current densities from 1 to 10 A g^{-1} are shown in Figure 8d. The specific capacitance of $Co_3O_4/ZnFe_2O_4$ from the discharge curves at larger current density of 2.5, 5, 7.5, and 10 A g^{-1} can be further calculated to be 254.5, 211.4, 189, 169 F g^{-1}, respectively. The capacitance of Co_3O_4, $ZnFe_2O_4$, and $Co_3O_4/ZnFe_2O_4$ electrodes exhibit 42.2%, 50%, and 51.8% retention from 1 to 10 A g^{-1}, due to the relatively slow faradic reactions.

With all these data, we calculate the single electrode energy density (E) and power density (P) from the energy density equation mentioned in introduction and following power density equation:

$$P = \frac{E}{\Delta t}$$

where Δt represents the electrode discharge time. The resulting energy and power densities ranging from 1 to 10 A g^{-1} are displayed in the Ragone plots of Figure 9a. With the potential window enlarged to 1.35 V, the energy density of the $Co_3O_4/ZnFe_2O_4$ electrode can reach 82.5 Wh kg^{-1} at a power density of 675 W kg^{-1}, significantly enhanced from the pure Co_3O_4 (17.8 Wh kg^{-1} at a power density of 250 W kg^{-1}) and $ZnFe_2O_4$ (40.4 Wh kg^{-1} at a power density of 722.5 W kg^{-1}) electrodes. Notably, the energy density of $Co_3O_4/ZnFe_2O_4$ still retained 44.3 Wh kg^{-1} with the power density as high as 6750 W kg^{-1}. The high power density with no massive energy density loss indicates that $Co_3O_4/ZnFe_2O_4$ has potential application in the smart supercapacitor field.[39]

The long-term cycle stability of supercapacitors is another key factor in practical use. As shown in Figure 9b, the cycling lifetime tests of 1000 cycles for Co_3O_4, $ZnFe_2O_4$ and $Co_3O_4/ZnFe_2O_4$ electrodes were carried out at 10 A g^{-1}. We can see the specific capacitance retention of 67.5%, 84.7%, and 80.7% was achieved after 1000 cycles. $ZnFe_2O_4$ showed the best retention among the three electrodes. With the presence of $ZnFe_2O_4$, $Co_3O_4/ZnFe_2O_4$'s cycling ability was dramatically improved from the pure Co_3O_4 electrode. It is worth noting that the charge/discharge curves are still symmetric after 1000 cycles test, indicating no significant structural changes of the $Co_3O_4/ZnFe_2O_4$ electrode during the charge/discharge processes.

Electrochemical impedance spectroscopy (EIS) was employed to further monitor the supercapacitors electrodes made of Co_3O_4, $ZnFe_2O_4$, and $Co_3O_4/ZnFe_2O_4$ in the frequency range from 10^5 to 10^{-2} Hz.

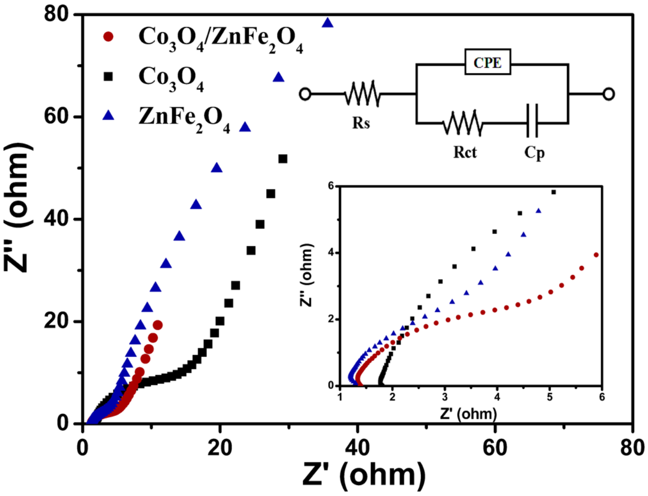

Figure 10. Nyquist plots of Co_3O_4, $ZnFe_2O_4$ and the starfish-shaped porous $Co_3O_4/ZnFe_2O_4$ in the frequency range from 10^5 to 10^{-2} Hz. The inset shows the high-frequency region of the Nyquist plot and equivalent circuit for the electrochemical impedance spectrum.

In Figure 10, the Nyquist plots of all electrodes are composed of a semicircle in the high frequency range and an oblique line in the low frequency range. Generally, the intercept in the Z′ axis represents the solution resistance, R_s, composed of the resistance of the electrolyte solution, the contact resistance at the interface between the current collector and the electroactive materials;[40] and the diameter of the semicircle is approximately equal to the charge transfer resistance, R_{ct}, through the electrode/electrolyte interface.[41] Electrode equivalent circuits can be simulated from the EIS data shown in the inset of Figure 10, and besides R_s and R_{ct}, it also includes a capacitor, C_p, and a constant phase element CPE. In this equivalent circuit mode, the R_s of the three electrodes are close to each other due to the same test conditions. However, the R_{ct} of the $Co_3O_4/ZnFe_2O_4$ electrode can be calculated to be 7.88 Ω, lying between the control Co_3O_4 and $ZnFe_2O_4$ electrodes. We suggest that the presence of $ZnFe_2O_4$ improves the charge transfer efficiency in the composite electrode.[42] Moreover, the trace amount of carbon observed from the XPS study might also contribute to this conductivity enhancement.

Generally, we believe the good capacitive performance of $Co_3O_4/ZnFe_2O_4$ electrode should be attributed to the following reasons: (i) the unique starfish-shaped structure of the $Co_3O_4/ZnFe_2O_4$. From the EIS analysis, we know the $ZnFe_2O_4$ has the smallest charge transfer resistance, R_{ct}. Therefore, in the starfish-shaped structure, the outlet "starfish arm" $ZnFe_2O_4$ nanotubes provide better and larger amounts of active sites for the electrons to penetrate through/into the inside "starfish head" Co_3O_4 nanocages, which possess better pseudocapacity as shown in CV diagrams. This novel structure can facilitate the synergistic effect of both Co_3O_4 and $ZnFe_2O_4$ and further achieve the best specific capacitance. (ii) The structure porosity brings large surface area and short diffusion paths in favor of the electrolyte ions and electrons transfer.[43] (iii) The innovative design of $Co_3O_4/ZnFe_2O_4$ mixing metal oxides expands the potential window to 1.35 V, resulting in enlarged energy and power densities.[44]

Magnetic Properties of Starfish-Shaped Porous $Co_3O_4/ZnFe_2O_4$ Nanocomposites. The magnetic properties of the bimagnetic $Co_3O_4/ZnFe_2O_4$ nanocomposite with starfish-shaped structure were measured on a superconducting quantum interference device (SQUID). The temperature dependences of the magnetic susceptibility (χ) for $Co_3O_4/ZnFe_2O_4$ under an applied field of 100 Oe are provided in Figure 11a. A ferromagnetic (FM) behavior is indicated apparently by the strong bifurcation of the ZFC and FC curves below $T \approx 30$ K, which is also evidenced by the magnetic hysteresis loops for nanocomposites at 1.8 K (Figure 11b). Above $T \approx 30$ K, zero-field-cooled (ZFC) and field-cooled (FC) curves become almost identical and increase slowly with decreasing temperature.

Figure 11b shows the magnetic hysteresis loops for as-synthesized $ZnFe_2O_4$ and $Co_3O_4/ZnFe_2O_4$ nanocomposites at 1.8 and 300 K. The approximately linear relationship between the magnetization (M) and magnetic field (H) implies that both $ZnFe_2O_4$ and $Co_3O_4/ZnFe_2O_4$ behave paramagnetically at 300 K. However, the hysteresis cycle measured at 1.8 K shows that the saturation magnetization (M_s) of $Co_3O_4/ZnFe_2O_4$ (27.5 emu g^{-1}) is lower than that of $ZnFe_2O_4$ (52.8 emu g^{-1}), which is possibly due to the decrease of the $ZnFe_2O_4$ component and the $Co_3O_4/ZnFe_2O_4$ size effect.[45] Meanwhile, it is worth noting the large coercivity (H_c = 884 Oe) and high squareness (M_r/M_s = 0.52) of $Co_3O_4/ZnFe_2O_4$ with respect to the $ZnFe_2O_4$ counterpart in Figure11c. As we all know, coercivity represents the system anisotropy;[46] however, since the anisotropy is strongly dependent on the particle morphology, size, surface effects, and interface exchange coupling effects,[47] it is difficult to predict the effective anisotropies of our $Co_3O_4/ZnFe_2O_4$ nanocomposites employing these limited data. With further detailed experiments in progress, here we qualitatively suggest that the enhancement of H_c and M_r/M_s of the $Co_3O_4/ZnFe_2O_4$ nanocomposites comes from the unique starfish-shaped nanostructure, which makes the high anisotropy available and leads to the surface and interface exchange coupling effects induced by the interfaces between the antiferromagnetic (AFM) Co_3O_4 nanocages and ferrimagnetic (FiM) $ZnFe_2O_4$ nanotubes.[48,49] This interesting observation might enlighten some prospective applications of this nanocomposite in magnetic devices.

■ CONCLUSIONS

In summary, we have demonstrated the rational design and fabrication of the starfish-shaped porous $Co_3O_4/ZnFe_2O_4$ hollow nanocomposites through a facile solid-state thermolysis of MOF precursors. The smart integration of Co_3O_4 and $ZnFe_2O_4$ realizes the synergistic effect between Co_3O_4 and

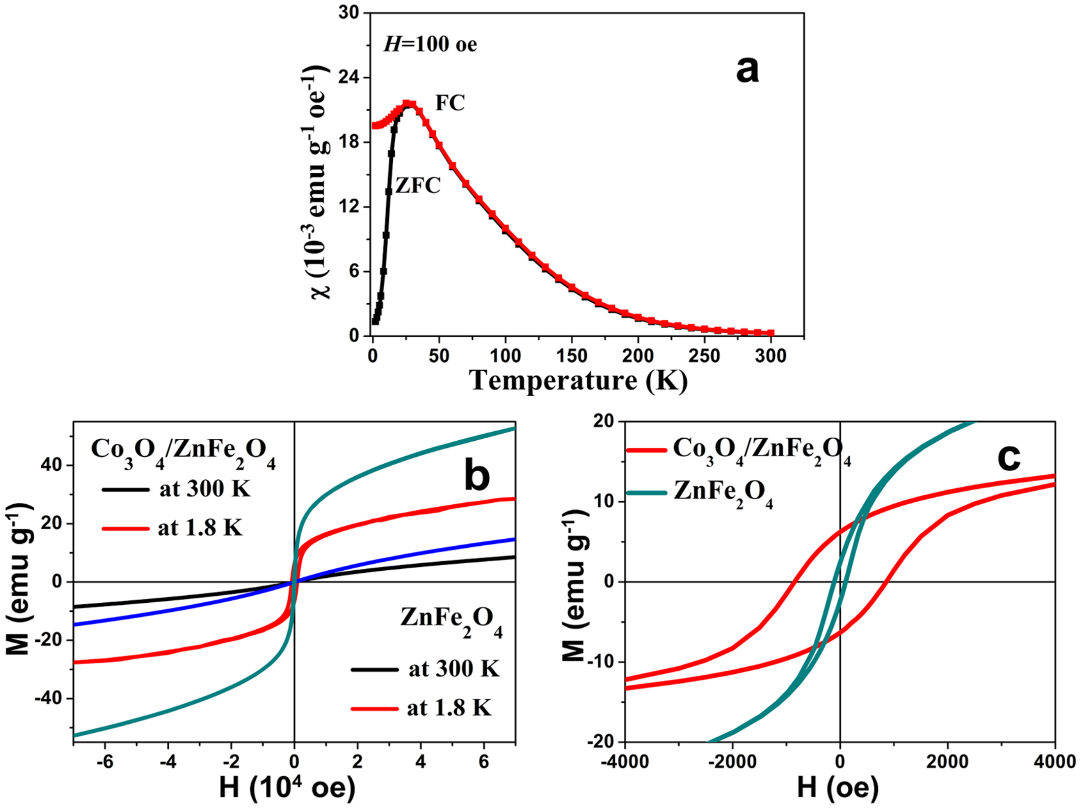

Figure 11. (a) Temperature dependence of magnetic susceptibility (χ) for $Co_3O_4/ZnFe_2O_4$ measured under an applied field of 100 Oe. (b) Magnetization hysteresis loops of $ZnFe_2O_4$ and $Co_3O_4/ZnFe_2O_4$ at 1.8 and 300 K. (c) Magnetization hysteresis loops of $ZnFe_2O_4$ and $Co_3O_4/ZnFe_2O_4$ at 1.8 K with a field range of −4000 to 4000 Oe.

$ZnFe_2O_4$. Moreover, the unique porous structure ensures sufficient penetration of the electrolyte and helps the enhanced electrode. The electrode made of $Co_3O_4/ZnFe_2O_4$ is able to work under a large potential window of 1.35 V, exhibiting good capacitive performance in terms of the energy density, specific capacity, and cycle life. The obtained highest energy density of 82.5 Wh kg^{-1} is achieved by $Co_3O_4/ZnFe_2O_4$ at a power density of 675 W kg^{-1}, which is much higher than that of the individual components. The large energy density at a high power delivery rate as well as the good cycle stability enable the starfish-shaped porous $Co_3O_4/ZnFe_2O_4$ to be a suitable electrode material for supercapacitor applications. Furthermore, the composite exhibits large coercivity and high squareness, compared to individual $ZnFe_2O_4$ at 1.8 K. The enhancement of the magnetic hysteresis loop may be attributed to the unique structure of $Co_3O_4/ZnFe_2O_4$ and the underlying surface and interface exchange coupling effects. This multifunctional material can be expected to have applications in both electrochemical energy storage and magnetic devices.

■ ASSOCIATED CONTENT

Ⓢ Supporting Information

Materials and reagents, preparation of Co_3O_4 nanocages, preparation of $ZnFe_2O_4$ hollow spheres, XRD pattern of the as-prepared $ZnFe_2O_4$ hollow spheres, TEM image of as-prepared $ZnFe_2O_4$ hollow spheres, CV curves for Co_3O_4, $ZnFe_2O_4$, and $Co_3O_4/ZnFe_2O_4$ with scanning rates of 5, 10, 20, 50, and 100 mV s^{-1}. This material is available free of charge via the Internet at http://pubs.acs.org.

■ AUTHOR INFORMATION

Corresponding Author

*Phone: +86 25 8359-2969, E-mail: youxz@nju.edu.cn (X.-Z.Y.).

Notes

The authors declare no competing financial interest.

■ ACKNOWLEDGMENTS

The work was supported in part by the National Natural Science Foundation of China (Nos. 21021062, 21271099 and 91022031) and National Basic Research Program of China (2013CB922100, and 2011CB808704). The authors gratefully acknowledge Prof. Y. Song and Dr. T. Wang for the helpful discussion on magnetic properties.

■ REFERENCES

(1) Conway, B. E. *Electrochemical Supercapacitors: Scientific Fundamentals and Technological Application*; Kluwer Academic/Plenum Publishers: New York, 1999.

(2) Lu, Q.; Chen, J. G.; Xiao, X. J. Nanostructured Electrodes for High-Performance Pseudocapacitors. *Angew. Chem., Int. Ed.* **2013**, *52*, 1882−1889.

(3) Yu, Z. Y.; Thomas, T. Energy Storing Electrical Cables: Integrating Energy Storage and Electrical Conduction. *Adv. Mater.* **2014**, *226*, 4279−4285.

(4) Choi, N. S.; Chen, Z. H.; Freunberger, S. A.; Ji, X. L.; Sun, Y. K.; Amine, K.; Yushin, G.; Nazar, L. F.; Cho, J.; Bruce, P. G. Challenges Facing Lithium Batteries and Electrical Double-Layer Capacitors. *Angew. Chem., Int. Ed.* **2012**, *51*, 9994−10024.

(5) Liu, S.; Sun, S.; You, X. Z. Inorganic Nanostructured Materials for High Performance Electrochemical Supercapacitors. *Nanoscale* **2014**, *6*, 2037−2045.

(6) Soin, N.; Roy, S. S.; Mitra, S. K.; Thundat, T.; Mclaughlin, J. A. Nanocrystalline Ruthenium Oxide Dispersed Few Layered Graphene (FLG) Nanoflakes as Supercapacitor Electrodes. *J. Mater. Chem.* **2012**, *22*, 14944−14950.

(7) Cheng, Y. W.; Lu, S. T.; Zhang, H. B.; Varanasi, C. V.; Liu, J. Synergistic Effects from Graphene and Carbon Nanotubes Enable Flexible and Robust Electrodes for High-Performance Supercapacitors. *Nano Lett.* **2012**, *12*, 4206−4211.

(8) Yuan, C.; Yang, L.; Hou, L.; Shen, L.; Zhang, X.; Lou, X. W. Growth of Ultrathin Mesoporous Co_3O_4 Nanosheet Arrays on Ni Foam for High-performance Electrochemical Capacitors. *Energy Environ. Sci.* **2012**, *5*, 7883−7887.

(9) Wang, B.; Chen, J. S.; Wang, Z.; Madhavi, S.; Lou, X. W. Green Synthesis of NiO Nanobelts with Exceptional Pseudo-Capacitive Properties. *Adv. Energy Mater.* **2012**, *2*, 1188−1192.

(10) Yan, J.; Wang, Q.; Wei, T.; Fan, Z. J. Recent Advances in Design and Fabrication of Electrochemical Supercapacitors with High Energy Densities. *Adv. Energy Mater.* **2013**, *4*, 1300816−1300858.

(11) Hu, C. C.; Chen, J. C.; Chang, K. H. Cathodic Deposition of $Ni(OH)_2$ and $Co(OH)_2$ for Asymmetric Supercapacitors: Importance of the Electrochemical Reversibility of Redox Couples. *J. Power Sources* **2013**, *221*, 128−133.

(12) Wang, Y. G.; Zhou, D. D.; Zhao, D.; Hou, M. Y.; Wang, C. X.; Xia, Y. Y. High Performance Hybrid Supercapacitor Based on Graphene-Supported $Ni(OH)_2$-Nanowires and Ordered Mesoporous Carbon CMK-5. *J. Electrochem. Soc.* **2013**, *160*, 98−104.

(13) Lee, J.; Farha, O. K.; Roberts, J.; Scheidt, K. A.; Nguyen, S. T.; Hupp, J. T. Metal−Organic Framework Materials as Catalysts. *Chem. Soc. Rev.* **2009**, *38*, 1450−1459.

(14) Li, J. R.; Kuppler, R. J.; Zhou, H. C. Selective Gas Adsorption and Separation in Metal−Organic Frameworks. *Chem. Soc. Rev.* **2009**, *38*, 1477−1504.

(15) Rosi, N. L.; Eckert, J.; Eddaoudi, M.; Vodak, D. T.; Kim, J.; O'Keeffe, M.; Yaghi, O. M. Hydrogen Storage in Microporous Metal-Organic Frameworks. *Science* **2003**, *300*, 1127−1129.

(16) An, J. Y.; Geib, S. J.; Rosi, N. L. Cation-Triggered Drug Release from a Porous Zinc−Adeninate Metal−Organic Framework. *J. Am. Chem. Soc.* **2009**, *131*, 8376−8377.

(17) Huxford, R. C.; DellaRocca, J.; Lin, W. B. Metal−Organic Frameworks as Potential Drug Carriers. *Curr. Opin. Chem. Biol.* **2010**, *14*, 262−268.

(18) Meek, S. T.; Greathouse, J. A.; Allendorf, M. D. Metal−Organic Frameworks: A Rapidly Growing Class of Versatile Nanoporous Materials. *Adv. Mater.* **2011**, *23*, 249−267.

(19) Wang, R. T.; Kong, L. B.; Lang, J. W.; Wang, X. W.; Fan, S. Q.; Luo, Y. C.; Kang, L. Mesoporous Co_3O_4 Materials Obtained from Cobalt−Citrate Complex and Their High Capacitance Behavior. *J. Power Sources* **2012**, *217*, 358−363.

(20) Xu, X. D.; Cao, R. G.; Jeong, S.; Cho, J. Spindle-like Mesoporous α-Fe_2O_3 Anode Material Prepared from MOF Template for High-Rate Lithium Batteries. *Nano Lett.* **2012**, *12*, 4988−4991.

(21) Zhang, L.; Wu, H. B.; Madhavi, S.; Hang, H. H.; Lou, X. W. Formation of Fe_2O_3 Microboxes with Hierarchical Shell Structures from Metal−Organic Frameworks and Their Lithium Storage Properties. *J. Am. Chem. Soc.* **2012**, *134*, 17388−17391.

(22) Zhang, F.; Hao, L.; Zhang, L. J.; Zhang, X. G. Solid-State Thermolysis Preparation of Co_3O_4 Nano/Micro Superstructures From Metal−Organic Framework for Supercapacitors. *Int. J. Electrochem. Sci.* **2011**, *6*, 2943−2945.

(23) Wang, H. L.; Gao, Q. M.; Hu, J. Asymmetric Capacitor Based on Superior Porous Ni−Zn−Co Oxide/Hydroxide and Carbon Electrodes. *J. Power Sources* **2010**, *195*, 3017−3024.

(24) Meng, F. L.; Fang, Z. L.; Li, Z. X.; Xu, W. W.; Wang, M. J.; Liu, Y. P.; Zhang, J.; Wang, W. R.; Zhao, D. Y.; Guo, X. H. Porous Co_3O_4 Materials Prepared by Solid-State Thermolysis of a Novel Co-MOF Crystal and Their Superior Energy Storage Performances for Supercapacitors. *J. Mater. Chem. A* **2013**, *1*, 7235−7241.

(25) Zou, F.; Hu, X. L.; Li, Z.; Qie, L.; Hu, C. C.; Zeng, R.; Jiang, Y.; Huang, Y. H. MOF-Derived Porous $ZnO/ZnFe_2O_4$/C Octahedra with Hollow Interiors for High-Rate Lithium-Ion Batteries. *Adv. Mater.* **2014**, *26*, 6622−6628.

(26) Hu, L.; Yan, N.; Chen, Q. W.; Zhang, P.; Zhong, H.; Zheng, X. R.; Li, Y.; Hu, X. Y. Fabrication Based on the Kirkendall Effect of Co_3O_4 Porous Nanocages with Extraordinarily High Capacity for Lithium Storage. *Chem.—Eur. J.* **2012**, *18*, 8971−8977.

(27) Zhang, Z. C.; Chen, Y. F.; Xu, X. B.; Zhang, J. C.; Xiang, G. L.; He, W.; Wang, X. Well-Defined Metal-Organic Framework Hollow Nanocages. *Angew. Chem., Int. Ed.* **2014**, *53*, 429−433.

(28) Qian, H. X.; Hu, Y.; Li, C. Q.; Yang, X. Y.; Li, L. C.; Zhang, X. T.; Xu, R. $ZnO/ZnFe_2O_4$ Magnetic Fluorescent Bifunctional Hollow Nanospheres: Synthesis, Characterization, and Their Optical/Magnetic Properties. *J. Phys. Chem. C* **2010**, *114*, 17455−17459.

(29) Wang, B.; Zhu, T.; Wu, H. B.; Xu, R.; Chen, J. S.; Lou, X. W. Porous Co_3O_4 Nanowires Derived from Llong $Co(CO_3)_{0.5}(OH)\cdot 0.11H_2O$ Nanowires with Improved Supercapacitive Properties. *Nanoscale* **2012**, *4*, 2145−2149.

(30) Guan, Q.; Cheng, J. L.; Wang, B.; Gu, G. F.; Li, X. D.; Huang, L.; Yang, G. C.; Nie, F. D. Needle-like Co_3O_4 Anchored on the Graphene with Enhanced Electrochemical Performance for Aqueous Supercapacitors. *ACS Appl. Mater. Interfaces* **2014**, *6*, 7626−7632.

(31) Low, Q. X.; Hoa, G. W. Facile Structural Tuning and Compositing of Iron Oxide−Graphene Anode Towards Enhanced Supacapacitive Performance. *Nano Energy* **2014**, *5*, 28−35.

(32) Haldoraia, Y.; Voitb, W.; Shima, J. J. Nano ZnO@Reduced Graphene Oxide Composite for High Performance Supercapacitor: Green Synthesis in Supercritical Fluid. *Electrochim. Acta* **2014**, *120*, 65−72.

(33) Zhang, L. L.; Zhao, X.; Stoller, M. D.; Zhu, Y. W.; Ji, H. X.; Murali, S.; Wu, Y. P.; Perales, S.; Clevenger, B.; Ruoff, R. S. Highly Conductive and Porous Activated Reduced Graphene Oxide Films for High-Power Supercapacitors. *Nano Lett.* **2012**, *12*, 1806−1812.

(34) Lei, Y.; Li, J.; Wang, Y. Y.; Gu, L.; Chang, Y. F.; Yuan, H. Y.; Xiao, D. Rapid Microwave-Assisted Green Synthesis of 3D Hierarchical Flower-Shaped $NiCo_2O_4$ Microsphere for High-Performance Supercapacitor. . *ACS Appl. Mater. Interfaces* **2014**, *6*, 1773−1780.

(35) Li, J. F.; Xiong, S. L.; Liu, Y. R.; Ju, Z. C.; Qian, Y. T. High Electrochemical Performance of Monodisperse $NiCo_2O_4$Mesoporous Microspheres as an Anode Material for Li-Ion Batteries. *ACS Appl. Mater. Interfaces* **2014**, *6*, 981−988.

(36) Lin, T. W.; Dai, C. S.; Hung, K. C. High Energy Density Asymmetric Supercapacitor Based on $NiOOH/Ni_3S_2$/3D Graphene and Fe_3O_4/Graphene Composite Electrodes. *Sci. Rep.* **2014**, *4*, 7274−7273.

(37) Tang, Z.; Tang, C. H.; Gong, H. A High Energy Density Asymmetric Supercapacitor from Nano-architectured $Ni(OH)_2$/Carbon Nanotube Electrodes. *Adv. Funct. Mater.* **2012**, *22*, 1272−1278.

(38) Ghosh, D.; Giri, S.; Moniruzzaman, M.; Basu, T.; Mandala, M.; Das, C. K. Alpha $MnMoO_4$/Graphene Hybrid Composite: High Energy Density Supercapacitor Electrode Material. *Dalton Trans.* **2014**, *43*, 11067−11076.

(39) Yang, D. F. Pulsed Laser Deposition of Cobalt-Doped Manganese Oxide Thin Films for Supercapacitor Applications. *J. Power Sources* **2012**, *198*, 416−422.

(40) Ramadoss, A.; Kim, S. J. Improved Activity of a Graphene−TiO_2 Hybrid Electrode in an Electrochemical Supercapacitor. *Carbon* **2013**, *63*, 434−445.

(41) Zhai, T.; Wang, F.; Yu, M.; Xie, S.; Liang, C.; Li, C.; Xiao, F.; Tang, R.; Wu, Q.; Lu, X.; Tong, Y. 3D MnO_2-Graphene Composites with Large Areal Capacitance for High-Performance Asymmetric Supercapacitors. *Nanoscale* **2013**, *5*, 6790−6796.

(42) Wang, Q.; Xu, J.; Wang, X.; Liu, B.; Hou, X.; Yu, G.; Wang, P.; Chen, D.; Shen, G. Core-Shell $CuCo_2O_4@MnO_2$ Nanowires on Carbon Fabrics as High-Performance Materials for Flexible, All-Solid-State, Electrochemical Capacitors. *ChemElectroChem.* **2014**, *1*, 559−564.

(43) Zhang, L.; Wu, H. B.; Xu, R.; Lou, X. W. Porous Fe_2O_3 Nanocubes Derived from MOFs for Highly Reversible Lithium Storage. *CrystEngComm* **2013**, *5*, 9332−9335.

(44) Qu, Q. T.; Yang, S. B.; Feng, X. L. 2D Sandwich-like Sheets of Iron Oxide Grown on Graphene as High Energy Anode Material for Supercapacitors. *Adv. Mater.* **2011**, *23*, 5574−5580.

(45) Ji, J. W.; Wang, G.; Wang, T. W.; You, X. Z.; Xu, X. W. Thiolate-Protected Ni_{39} and Ni_{41} Nanoclusters: Synthesis, Self-assembly and Magnetic Properties. *Nanoscale* **2014**, *6*, 9185−9191.

(46) Chetri, P.; Basyach, P.; Choudhury, A. Exploring the Structural and Magnetic Properties of TiO_2/SnO_2 Core/Shell Nanocomposite: An Experimental and Density Functional Study. *J. Solid State Chem.* **2014**, *220*, 124−131.

(47) Jr, E. L.; Winkler, E. L.; Tobia, D.; Troiani, H. E.; Zysler, R. D.; Agostinelli, E.; Fiorani, D. Bimagnetic CoO Core/$CoFe_2O_4$ Shell Nanoparticles: Synthesis and Magnetic Properties. *Chem. Mater.* **2012**, *24*, 512−516.

(48) Sun, S.; Zeng, H.; Robinson, D. R.; Raoux, S.; Rice, P. M.; Wang, S. X.; Li, G. Monodisperse MFe_2O_4 (M = Fe, Co, Mn) Nanoparticles. *J. Am. Chem. Soc.* **2004**, *126*, 273−279.

(49) Skumryev, V.; Stoyanov, S.; Zhang, Y.; Hadjipanayis, G.; Givord, D.; Nogués, J. Beating the Superparamagnetic Limit with Exchange Bias. *Nature* **2003**, *423*, 850−853.